**Citation (APA)**
Correia, A. S., Mazza, F., Castellanos, L., Rao, A. G., & De Domenico, F. (2026). Spatially resolved flame front marker using the temperature dependence of OH PLIF excitation lines. *International Journal of Hydrogen Energy*, *247*, Article 155740. https://doi.org/10.1016/j.ijhydene.2026.155740

International Journal of Hydrogen Energy 247 (2026) 155740

Contents lists available at ScienceDirect

International Journal of Hydrogen Energy

journal homepage: www.elsevier.com/locate/he

# Spatially resolved flame front marker using the temperature dependence of OH PLIF excitation lines

André Silva Correia [a,*], Francesco Mazza [a,b], Leonardo Castellanos [a], Arvind Gangoli Rao [a], Francesca De Domenico [a]

[a] *Faculty of Aerospace Engineering, Delft University of Technology, 2629HS Delft, The Netherlands*
[b] *Process and Chemical Engineering, RWTH Aachen University, 52062 Aachen, Germany*

## ARTICLE INFO

*Keywords:*
Hydrogen
Flame front marker
Spatial resolution
OH PLIF
Two-line PLIF

## ABSTRACT

Flame front identification typically relies on chemiluminescence or planar laser-induced fluorescence (PLIF) diagnostics. Yet, existing approaches are often limited by line-of-sight integration, low signal-to-noise ratio, or limited applicability to hydrogen flames. This study introduces a novel OH PLIF-based method that isolates the flame front by subtracting fluorescence signals obtained from two excitation lines with distinct temperature dependencies. The method is validated using LIFSIM coupled with 1D freely propagating flame simulations and is experimentally demonstrated in a laminar premixed $H_2$-air Bunsen flame. The resulting flame front marker exhibits a well-defined peak located, on average, 0.56 flame thicknesses from the heat release rate (HRR) peak and an average width of 1.57 times the HRR width. These values are comparable to those obtained from $OH^*$ chemiluminescence and the OH PLIF gradient, while offering substantially higher SNR and providing spatial resolution. Beyond introducing a new flame-front marker, suitable for hydrogen flames, this work provides a numerical and experimental assessment of OH-based HRR markers, evaluating their performance for hydrogen flame diagnostics.

## 1. Introduction

Global energy production and consumption remain heavily dependent on the combustion of fossil fuels for powering transport, heating and electricity generation, which together account for a significant share of global greenhouse gas emissions [1]. Transitioning these energy systems to carbon-free fuels is therefore essential to meet net-zero emission targets. Among the available alternatives, hydrogen ($H_2$) has emerged as a leading candidate fuel due to its high energy content, wide flammability limits and absence of carbon-based emissions. However, $H_2$ combustion properties – namely higher flame speed [2] and diffusivity [3] compared to hydrocarbon fuels, as well as increased autoignition propensity [4,5] – contribute to increased flashback risk and propensity for thermo-diffusive, and thermo-acoustic instabilities. Understanding these phenomena is fundamental, as they strongly influence fuel efficiency and pollutant formation in modern combustion systems [6].

Developing stable and efficient $H_2$ combustion systems requires precise and high-resolution information on the flame front behaviour and its associated heat release rate (HRR). This stems from the fact that flame front dynamics, such as wrinkling, local quenching and displacement, directly reflect these instabilities, and the HRR is intrinsically linked to the instantaneous flame front location and structure. Therefore, accurate detection of the flame front is crucial to investigate such instabilities and allows the design of stable, efficient $H_2$ combustors [7–9]. Yet, the absence of carbon in hydrogen flames complicates the use of established diagnostics and their interpretation. As a result, considerable effort has recently been devoted to develop diagnostic and data analysis methods capable of capturing the behaviour of $H_2$ flames [10–20].

Experimental studies have examined the stability of lean premixed hydrogen flames, revealing that hydrogen diffusivity can lead to cellular instabilities, local quenching, and flame front wrinkling, using diagnostics like high-speed Schlieren and laser-induced fluorescence (LIF) [10–12]. Moreover, dominant frequency modes correlating with heat release fluctuations have been identified as contributors to thermoacoustic instabilities, using tools such as spectral proper orthogonal decomposition (SPOD), power spectral density (PSD) and flame transfer function (FTF), as well as pressure measurements [13–15]. In parallel with these studies, new combustor concepts such as dual-swirl injectors and micromix burners have been introduced to stabilise $H_2$ flames

---

* Corresponding author.
*E-mail address:* A.SilvaCorreia@tudelft.nl (A.S. Correia).

https://doi.org/10.1016/j.ijhydene.2026.155740
Received 9 February 2026; Received in revised form 11 May 2026; Accepted 24 May 2026

while controlling $NO_x$ emissions, although these configurations remain susceptible to longitudinal and thermoacoustic instabilities [16–18]. On the modelling side, large-eddy simulation (LES) models incorporating thermodiffusive effects have emerged, providing detailed predictions of flame structure and heat release. However, their accuracy ultimately depends on experimental validation of flame front dynamics and heat release characteristics [19,20].

In hydrocarbon flames, this experimental validation often relies on combustion radicals such as OH*, CH*, $C_2$* and $CO_2$*, which are employed as tracers of heat release to analyse flame structure through their chemiluminescence [21–23]. In $H_2$ flames, however, only OH* is present and therefore serves as the primary marker of heat release. Yet, its emission is weaker than in methane ($CH_4$) flames, and numerical simulations show a larger peak-to-peak distance between OH* and the actual HRR [24,25]. Several studies have therefore examined the suitability of OH* as a HRR marker [26,27], and while it is less reliable in premixed $H_2$-air flames than in diffusion flames, it remains widely used due to the simplicity of its diagnostic setup. In practice, it requires only a UV-sensitive camera and a band-pass filter centred at 308 nm, corresponding to the $A^2\Sigma^+$-$X^2\Pi$ (0,0) vibronic emission band. While straightforward, the technique inherently provides line-of-sight integrated measurements, limiting spatial resolution. Tomographic reconstruction [28] and Abel inversion [29] can mitigate this limitation in axisymmetric flames, however, these approaches are unsuitable for turbulent or non-axisymmetric flames. Moreover, the exposure times required to capture sufficient light (e.g. 100 μs) compromise temporal resolution [30], making it difficult to resolve fast transient phenomena such as flame wrinkling or local quenching in hydrogen flames.

Laser-based techniques, such as LIF, are commonly employed to overcome the limited spatial and temporal resolution of line-of-sight measurements. LIF relies on the excitation of a target molecule through a specific electronic and ro-vibrational transition [31], followed by emission of light when the molecule relaxes and releases a photon. Spatially resolved measurements are achieved by shaping the laser into a sheet using cylindrical lenses, enabling the acquisition of planar sections of the flame (planar laser-induced fluorescence, PLIF). Fluorescence occurs on a timescale of a few tens of nanoseconds [32], thus the exposure can be as short as 100 ns, yielding a temporal resolution shorter than the Kolmogorov timescale (the shortest turbulence timescale).

Common target molecules for flame front identification include hydroxyl (OH) and formaldehyde ($CH_2O$). The latter is an intermediate species formed in the preheat zone and a precursor to formyl radical (HCO), a strong indicator for HRR in hydrocarbon flames [33]. In such flames, to achieve a signal that correlates with HCO, $CH_2O$ PLIF is often multiplied by OH PLIF, effectively highlighting the flame front [34–36]. However, this approach cannot be applied to $H_2$ combustion, where no carbon species are present, leaving OH as the only practical LIF tracer. OH PLIF, in contrast, provides both spatial and temporal resolution for flames containing both hydrogen and oxygen atoms, including hydrocarbons and $H_2$ flames. Yet, since OH is present in both the reaction zone and the post-flame region, its fluorescence represents this entire region rather than specifically marking the flame front. Although this does not pose a limitation in well-defined laminar flames, in turbulent flames OH can diffuse into unburnt regions, potentially leading to misinterpretation of the flame location. The OH fluorescence gradient (∇OH) can nevertheless be used to retrieve the flame edge by identifying its maximum [37], however, it typically suffers from low signal-to-noise ratio (SNR) and strong spatial non-uniformities, making the post-processing challenging [38,39].

In response to the aforementioned diagnostic challenges associated with $H_2$ flames, this study proposes an alternative OH PLIF-based method for spatially resolved flame front detection in hydrogen flames. While demonstrated here in a premixed $H_2$-air laminar Bunsen flame as proof of concept, the method is designed to be extendable to time-resolved measurements and non-axisymmetric, turbulent conditions. Similar to two-line PLIF [40], this approach exploits the temperature dependence of different excitation lines. Rather than using their ratio to measure temperature, the method creates a marker across the reaction zone by subtracting the fluorescence signals from two excitation lines with distinct temperature dependencies. To identify suitable excitation lines, the temperature dependence is determined using LIFSIM [41] in combination with the OH number density obtained from a 1D freely-propagating $H_2$-air flame simulation with CANTERA [42]. These simulations are also used to validate and characterise the spatial distance between the proposed marker's peak and the peak of HRR, as well as the marker's width relative to that of HRR, in comparison with existing techniques (OH* and ∇OH). Experimental results confirmed the feasibility of the method in a premixed $H_2$-air Bunsen flame and allowed direct comparison with the other techniques, leading to the first systematic numerical and experimental assessment of OH-based HRR markers in hydrogen flames. Due to the availability of a single laser system, these results were obtained by acquiring the fluorescence from the two excitation line sequentially. This approach was considered feasible due to the steady nature of the laminar flames employed, which enabled the use of averaged images.

The paper is structured as follows: Section 2 details the numerical and experimental methodology, including the selection of the spectral lines based on the temperature dependence of OH LIF and the use of 1D freely-propagating flames to numerically validate the proposed approach. The experimental setup and the post-processing algorithm used to retrieve the peak location and width of the markers from the acquired images are also discussed. Section 3 presents the experimental results and compares the proposed method with OH* chemiluminescence and OH PLIF gradient. Finally, Section 4 discusses future perspectives of the proposed method, while Section 5 summarises the key findings of the study.

## 2. Methodology

This section outlines the numerical and experimental steps used to characterise and validate the proposed flame-front marker. It starts with discussing 1D freely propagating $H_2$-air flame simulations, which provide the temperature and species profiles used throughout the study. These profiles are then coupled with detailed OH fluorescence calculations to identify two excitation lines with distinct temperature dependencies, allowing the subtraction marker ((−)OH) to be obtained. The method is subsequently evaluated by computing fluorescence profiles using the selected transitions and comparing them with established markers such as OH* and ∇OH. The experimental setup used to acquire OH PLIF and OH* chemiluminescence is then introduced, followed by the image-processing algorithm applied to the OH*, (−)OH and ∇OH to extract peak locations and peak widths. Together, these steps establish a consistent framework to evaluate the behaviour of the three markers across different equivalence ratios under both numerical and experimental conditions.

### 2.1. Numerical simulation of freely propagating flames

1D simulations of freely-propagating premixed $H_2$-air laminar flames were performed for equivalence ratios of $0.5 < \phi < 1.3$. These simulations were achieved using CANTERA [42] with the GRI-3.0 reaction mechanism [43], along with the OH* reaction mechanisms proposed by Kathrotia et al. [44], which has been widely used as a reference in hydrogen flames [26,27,45–47]. Furthermore, the multicomponent transport model accounting for diffusive mass fluxes due to the Soret effect was applied. The following governing equations were solved:

*(Continuity)*

$$\frac{d}{dz}(\rho u) = 0 \tag{1}$$

*(Energy)*

$$\frac{d}{dz}(\rho u h) = \frac{d}{dz}\left(\kappa \frac{dT}{dz}\right) - \sum_k j_k \frac{dh_k}{dz} \tag{2}$$

*(Species)*

$$\frac{d}{dz}(\rho u Y_k) = -\frac{dj_k}{dz} + W_k \dot{\omega}_k \tag{3}$$

where $\rho$ is the density, $u$ is the velocity, $z$ is the spatial coordinate, $h$ is the specific enthalpy, $\kappa$ is the thermal conductivity, $T$ is the temperature, $j_k$ is the diffusive mass flux of the species $k$, $h_k$ the enthalpy of the species $k$, $Y_k$ is the mass fraction of the species $k$, $W_k$ is the molecular weight of the species $k$ and $\dot{\omega}_k$ the molar production rate of the species $k$. The *momentum* equation is not included, as it is redundant for subsonic flows where the pressure remains nearly constant, as in freely propagating flames.

Even though these 1D simulations do not fully represent a Bunsen flame, due to curvature at the base and the tip, they accurately describe the quasi-planar, unstrained region of the flame. This region is used to determine the peak position and width, as described in Section 2.5. In the present study, the deviation of the evaluated region from the a planar assumption is up to 0.015 mm, even under richer conditions where, assuming constant thermal power, the flame volume decreases. This supports the validity of using 1D simulations to describe the quasi-planar region.

In addition to providing OH number density profiles to aid the line selection (Section 2.2), the simulations were also used to compute HRR and OH* profiles. These profiles allow a numerical comparison between the different markers, as detailed in Section 2.3.

### 2.2. Temperature dependence of OH fluorescence spectra

The proposed method relies on creating a marker across the flame front by subtracting the fluorescence signals resulting from two OH excitation lines with distinct temperature dependencies. To effectively isolate the thin reaction zone, this distinction needs to be maximised by selecting the least and the most temperature-dependent lines. To evaluate this dependency, the OH fluorescence excitation spectrum must be accurately computed over a range of temperatures. This was performed using LIFSIM [41] since it provides high modularity and user control over the simulation parameters necessary to this study. Specifically, the ability to disable the standard spectrum normalisation allows to accurately compare absolute line intensities across different simulations and therefore the temperature dependency of each line. LIFSIM integrates all emissions following absorption at a given excitation wavelength, corresponding to the energy difference between the lower and upper energetic state. The fluorescence intensity is determined following [41], where three parameters are identified as temperature-dependent: the *Boltzmann distribution* ($f_B$), the *line overlap integral* ($\Gamma_{\tilde{\nu}}$), and the *quenching rate* ($Q_k$).

The *Boltzmann distribution* describes the probability of a molecule to reside in a specific quantum state of energy $E_i$ and is expressed as

$$f_B = \frac{2J'' + 1}{Z} e^{-\frac{E_i}{kT}} \tag{4}$$

where $J''$ is the rotational quantum number of the lower state, $Z$ is the partition function, $E_i$ is the ground state energy, $k$ is the Boltzmann constant, and $T$ is the temperature. With increasing temperature, higher rotational states become more populated, resulting in a red-shifted redistribution of the fluorescence spectrum.

The *line overlap integral* quantifies the spectral match between the laser line shape and the absorption line shape of the molecule. The latter is described by a Voigt function, a convolution of Gaussian and Lorentzian profiles [31]. The Gaussian profile is subject to Doppler broadening, which scales with temperature. Higher temperatures broaden the absorption lines, increasing the overlap between neighbouring transitions. This reduces the selectivity of single absorption lines, as the laser may partially excite adjacent transitions. This broadening was quantified to be on the order of 2 pm over the investigated temperature range (1100–2400 K). As it will be shown later, this effect is negligible compared to the separation between available OH transitions, ensuring that individual lines remain resolvable.

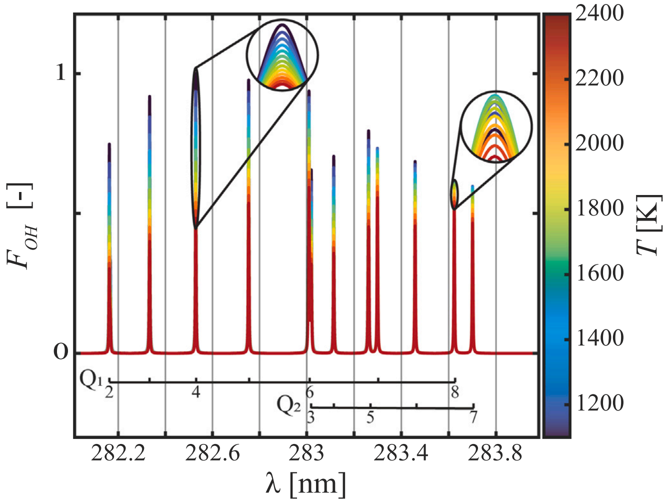

**Fig. 1.** Effect of temperature on the OH A-X(1,0) fluorescence spectrum simulated with LIFSIM. Transitions with relative intensity below 50.8% of the maximum at 2400 K were excluded due to poor SNR (< 10).

The *quenching rate* $Q_k$ quantifies the loss of energy of the excited molecules through collisions with surrounding species rather than by photon emission. The quenching rate is inversely proportional to temperature and is expressed as

$$Q_k = \frac{p}{kT} \sum_r x_r v_r \sigma_r(T) \tag{5}$$

where $p$ is pressure, $x_r$ is the mole fraction of the collision partner $r$, $v_r$ is the average collision velocity and $\sigma_r$ is the collisional cross-section. For OH as the target molecule, $\sigma_r$ also decreases with increasing temperature [48]. As a result, higher temperatures reduce collisional quenching, having a positive impact on fluorescence intensity. Furthermore, since $\sigma_r$ varies primarily between different vibrational bands [49] and this work considers only the OH A-X (1,0) band, its effect is uniform across all excitation lines and therefore does not influence line selection. Thus, to simplify the analysis, collisional quenching was neglected in this study, as OH quenching models are not yet implemented in LIFSIM [41].

The OH A-X (1,0) fluorescence spectrum shown in Fig. 1 was generated using LIFSIM over the temperature range in which OH is present in a $H_2$-air flame (1100–2400 K). This vibronic band corresponds to the transitions from the first excited electronic state and the first excited vibrational state, A(1), to the ground electronic and vibrational state, X(0). A homogeneous media with unit OH number density ($N_{OH} = 1$) was assumed. The spectrum was restricted to the tunable wavelength range of the laser (282–284 nm, see Section 2.4), and a threshold of 50.8% of the maximum at 2400 K was applied, as the lines below this level showed poor SNR (< 10) in the experimental peak scan.

Fig. 1 also illustrates how the intensity of each excitation line varies with temperature. For instance, $Q_1(4)$, despite being one of the lines with the highest intensity at $T = 1100$ K, decreases significantly with temperature, with a reduction of 52% relative to the intensity at $T = 1100$ K, whereas $Q_1(8)$ remains relatively stable, reducing by only 13%. Furthermore, the two insets highlight a common misconception, namely that the increase of temperature leads to a uniform decrease in the signal. Although this is true for the overall integral of the spectrum,

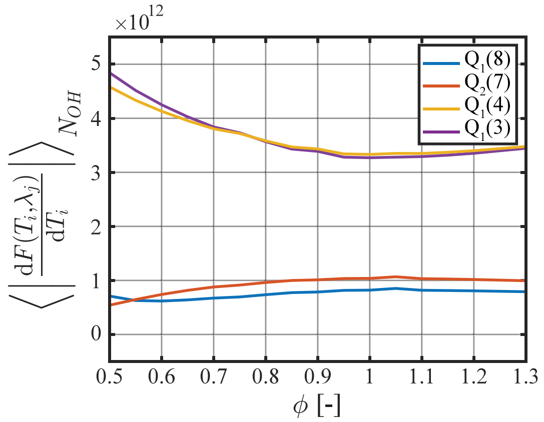

**Fig. 2.** Temperature dependence of different fluorescence excitations wavelengths across $\phi$. OH A-X(1,0) $Q_1(8)$ and $Q_2(7)$ represent the least temperature-dependent lines and $Q_1(3)$, $Q_1(4)$ the most temperature-dependent ones.

it does not apply to every individual line. For example, the intensity of the $Q_1(8)$ transition increases up to 1500 K before it begins to decrease.

As established at the beginning of this section, the proposed method relies on subtracting OH PLIF signals obtained from two excitation lines with distinct temperature dependencies. Consequently the most and least temperature-dependent excitation lines should be selected. To this end, a metric was defined based on the fluorescence intensity at different temperatures, weighted by the OH number density obtained at the corresponding temperatures from the 1D freely propagating premixed $H_2$-air flame simulation (see Section 2.1) at a given equivalence ratio ($\phi$):

$$\left\langle \left| \frac{\mathrm{d}F(T_i,\lambda_j)}{\mathrm{d}T_i} \right| \right\rangle_{N_{OH}} \tag{6}$$

where $F(T_i,\lambda_j)$ is the fluorescence at the $i$th temperature, $T_i$, and at the $j$th excitation line, $\lambda_j$. This weighting emphasises the temperature dependence in regions where OH is more abundant, ensuring that the selected excitation lines are relevant to the flame conditions being studied. This analysis was performed using the open-source tool LIFTempDependence [50]. Applying this approach across equivalence ratios from 0.50 to 1.30 shows that $Q_1(8)$ is the least temperature-dependent line for $\phi = 0.55$-1.30, consistent with the findings of Tu et al. [51], while $Q_2(7)$ becomes the least temperature-dependent line at $\phi = 0.50$. The most temperature-dependent line is $Q_1(4)$ at $\phi = 0.75$-1.30, and $Q_1(3)$ for the remaining equivalence ratios, although their dependence differs by less than 5.7%. This can be observed in Fig. 2, where the weighted temperature dependence of selected lines is plotted against the equivalence ratio.

Although selecting a different pair for each condition could maximise the temperature contrast and thus modify the peak location and peak width (as measured in Section 2.3), the difference between selecting any line pair in {$Q_1(8)$,$Q_2(7)$} and {$Q_2(3)$,$Q_2(4)$} was quantified to be below 2% across all conditions. Therefore, to ensure a consistent trend and avoid variations arising from changing the excitation line pairs across equivalence ratios, $A^2\Sigma^+$-$X^2\Pi$ (1,0) $Q_1(8)$ at 283.636 nm and $A^2\Sigma^+$-$X^2\Pi$ (1,0) $Q_1(4)$ at 282.522 nm were selected as the least and most temperature-dependent excitation lines, respectively.

### 2.3. *Method development*

As mentioned in the Section 1, this work proposes an alternative approach for highlighting the flame front in $H_2$ flames by subtracting the OH fluorescence signals obtained from the most and least temperature-dependent excitation lines. To validate this approach, the 1D flame simulations described in Section 2.1 were used to retrieve temperature and OH number-density ($N_{\mathrm{OH}}$) spatial profiles across a range of $\phi$. These profiles were then coupled with LIFSIM using the excitation lines selected in Section 2.2. This coupling first required computing the line intensities over the studied temperatures (1100–2400 K) in a homogeneous media, generating a manifold for each excitation line. At each point of the flame simulation grid, the respective OH fluorescence was computed by multiplying the local $N_{\mathrm{OH}}$ with the line intensity at the corresponding temperature, as $F_{\mathrm{OH}}(\lambda,T) = N_{\mathrm{OH}} I(\lambda,T)$. This allowed to evaluate the expected OH fluorescence across the flame for each excitation line, followed by the normalisation and subtraction of the two fluorescence profiles. This normalisation step is required to remove absolute intensity differences between excitation wavelengths, such that the subtraction emphasises differences in the local rate of signal increase across the flame front rather than their absolute magnitude. Fig. 3(a) displays examples of the resulting (−)OH marker together with the simulated HRR, as well as the individual OH fluorescences signals from the most and the least temperature-dependent excitation wavelengths, for $\phi = 0.50$, 1.00 and 1.30. For reference, the OH* concentration and the ∇OH are also included, as these quantities are commonly used as markers for heat release and flame front [37,52]. Both will later serve as benchmarks for the proposed method in the numerical and the experimental analysis. These results provide preliminary evidence that subtracting two fluorescence signals, excited from excitation lines with different temperature dependencies, effectively creates a marker across the flame front. Fig. 3(b) summarises the relative peak position of these markers with respect to the HRR across the equivalence ratio range, showing that at lean conditions, (−)OH lies closer to the HRR and ∇OH, while at rich conditions it drifts towards the OH* peak. These peaks are determined by identifying the highest local maxima of each profile in Fig. 3(a) (HRR, (−)OH, OH* and ∇OH). Both (−)OH and ∇OH exhibit secondary peaks in richer flames which arise from a small shoulder in the fluorescence profile due to atomic hydrogen diffusion [53,54]. However, for this range of $\phi$, these secondary peaks never exceed the main maximum and can therefore be disregarded in the analysis.

The relative proximity of each marker to the HRR is further illustrated in Fig. 4(a), which presents the peak-to-peak distance relative to HRR, normalised by the laminar flame thickness $\delta_L^0 = (T_{max} - T_{min})/\max(\nabla T)$, obtained from the 1D simulations in Section 2.1. Over the studied equivalence ratios, (−)OH remains 0.15-0.65 $\delta_L^0$ away from the HRR peak, while OH* lies within 0.34-0.60 $\delta_L^0$ and ∇OH at 0.10-0.21 $\delta_L^0$, being the closest.

The peak widths of the markers, taken at full width at half maximum (FWHM), relative to HRR are shown in Fig. 4(b). With the increase of equivalence ratio, (−)OH becomes broader, going from 1.3 and reaching up to 5.6 times the HRR width. OH* also broadens at rich conditions, despite staying within a factor of 0.90 to 2.3 of the HRR width. The ∇OH marker shows a decrease in width with equivalence ratio, but remains narrower than HRR, 0.65 to 0.74 of its width. These trends highlight that none of the methods provide a perfect match to HRR. The discrepancy becomes more pronounced in practical applications, where the line-of sight integration in OH* (even when Abel-inverted), the limited SNR of ∇OH [38,39], non-adiabatic conditions and limited camera resolution all contribute to reduced experimental accuracy. This will be demonstrated later in the Section 3, where the markers obtained from OH* and ∇OH are compared with the proposed (−)OH marker. It should be noted that these numerical results are not intended to fully reproduce the experimental results, but rather to assess the viability of the (−)OH marker under simplifying conditions and compare it to OH* and ∇OH.

### 2.4. *Experimental setup*

To validate the proposed method, a premixed $H_2$-air laminar flame was achieved in a Bunsen burner of 4 mm inner diameter and a length-to-diameter ratio of approximately 100:1. The fuel and oxidiser flows

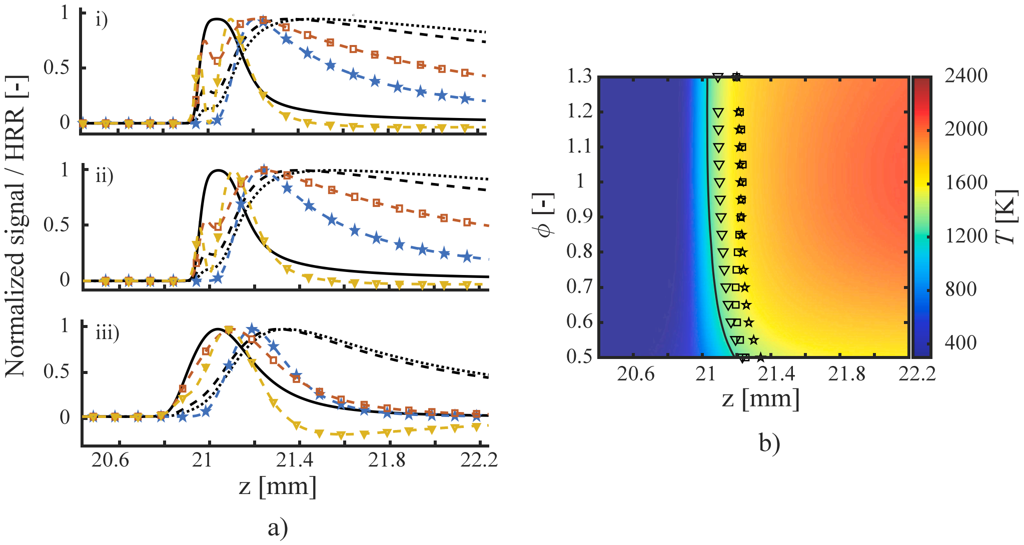

**Fig. 3.** (a) Normalised HRR (——), (−)OH (-□-), OH fluorescence from $Q_1(4)$ (- - -) and $Q_1(8)$ (·····) transitions, OH* mass fraction (-☆-), and ∇OH (-▽-) distributions obtained from a 1D simulation of freely propagating premixed $H_2$–air laminar flames at $\phi = 0.5$, 1.0 and 1.3 (i, ii and iii, respectively). (b) Corresponding peak locations of HRR (——), (−)OH (□), OH* (☆) and ∇OH (▽) overlaid on the temperature contour for $\phi = 0.5 - 1.3$.

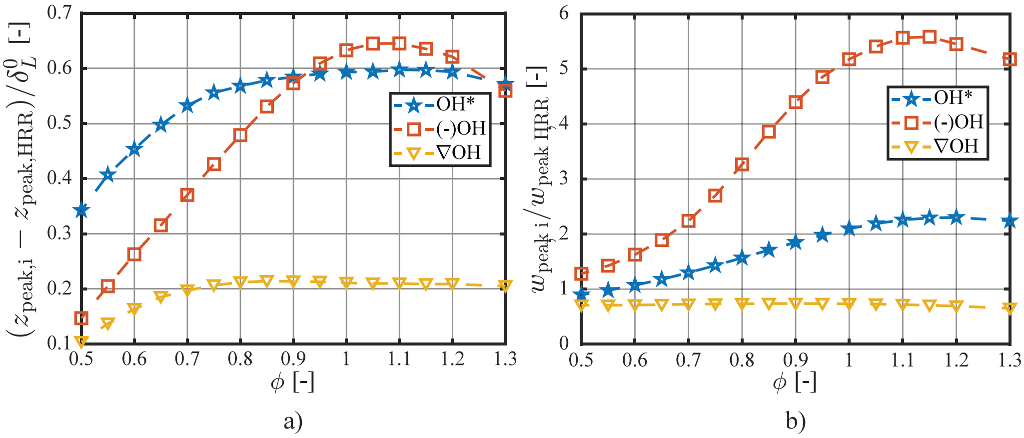

**Fig. 4.** (a) Normalised peak-to-peak distance and (b) normalised peak-width of (−)OH, OH* and ∇OH relative to HRR obtained from freely propagating premixed $H_2$–air laminar flames coupled with LIFSIM [41] over $\phi = 0.5 - 1.3$.

were controlled independently using thermal mass-flow controllers (Bronkhorst F-201AV and F-202AV, respectively) with an accuracy of ±0.5% of the reading, plus ±0.1% of the full scale. Test conditions are listed in Table 1, covering equivalence ratios ranging from 0.50 (fuel-lean) to 1.30 (fuel-rich) in 0.05 increments, except for 1.25. Leaner flames could not be stabilised due to burner limitations, while richer conditions resulted in a dual flame structure: a premixed central flame surrounded by an outer diffusion flame, where the excess fuel reacts with the entrained ambient air. Under these richer conditions, OH production dominated in the outer diffusion flame, causing the OH fluorescence signal from the premixed flame to fade into the background noise and become indistinguishable. Such conditions were therefore excluded from the study. Mass-flow rates were adjusted to maintain constant thermal power of 250 W, leading to an increasing cone angle with equivalence ratio.

The OH excitation was achieved using the second harmonic of a tunable dye laser (Sirah CobraStretch G 30) with Rhodamine 6G dissolved in ethanol, pumped by the second harmonic of an Nd:YAG laser (Q-smart 850). This configuration provided an output of 14 mJ/pulse at the output of the dye laser, with a spectral width of 2 pm over a 282–284 nm range, covering most of the rotational transition with significant amplitude in the $A^2\Sigma^+$-$X^2\Pi$ (1,0) vibrational band of OH.

**Table 1**

$H_2$-air premixed laminar flame experimental conditions.

| $\phi$ | $\dot{m}_{H_2}$ [$\times10^{-6}$ kg/s] | $\dot{m}_{air}$ [$\times10^{-6}$ kg/s] |
|---|---|---|
| 0.50 | 2.08 ± 0.099 | 143 ± 2.00 |
| 0.55 | 2.08 ± 0.099 | 130 ± 1.94 |
| 0.60 | 2.08 ± 0.099 | 119 ± 1.89 |
| 0.65 | 2.08 ± 0.099 | 110 ± 1.84 |
| 0.70 | 2.08 ± 0.099 | 102 ± 1.80 |
| 0.75 | 2.08 ± 0.099 | 95.0 ± 1.77 |
| 0.80 | 2.08 ± 0.099 | 89.1 ± 1.74 |
| 0.85 | 2.08 ± 0.099 | 83.8 ± 1.71 |
| 0.90 | 2.08 ± 0.099 | 79.2 ± 1.69 |
| 0.95 | 2.08 ± 0.099 | 75.0 ± 1.67 |
| 1.00 | 2.08 ± 0.099 | 71.3 ± 1.65 |
| 1.05 | 2.08 ± 0.099 | 67.9 ± 1.63 |
| 1.10 | 2.08 ± 0.099 | 64.8 ± 1.62 |
| 1.15 | 2.08 ± 0.099 | 62.0 ± 1.60 |
| 1.20 | 2.08 ± 0.099 | 59.4 ± 1.59 |
| 1.30 | 2.08 ± 0.099 | 54.8 ± 1.57 |

Imperfections in the laser beam profile were removed using an iris before focusing the beam through two cylindrical lenses to form a laser sheet. A telescope lens was then used to adjust the focal length

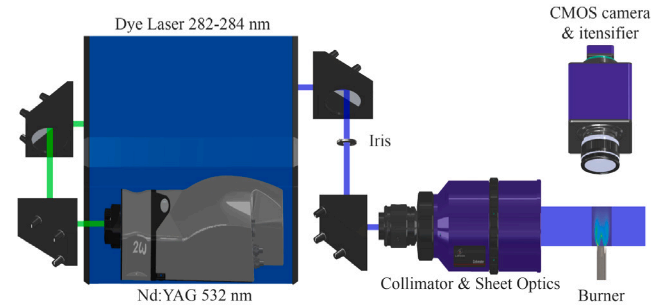

**Fig. 5.** Schematic of the experimental setup and diagnostics used in this work. The system includes an Nd:YAG laser pump laser, a tunable dye laser, an iris, sheet optics, an intensified CMOS camera and a 4 mm Bunsen burner. Dimensions are not to scale.

to ensure that the probe volume remained within the Rayleigh length of the sheet, with the focus centred on the target. To optimise the intensity distribution along the laser height, a converging lens was placed before the second cylindrical lens, allowing the collimation of the sheet in the vertical plane. This resulted in a 56.3 mm high and 167 $\mu$m wide laser sheet, which was characterised using a beam profiler (WinCamD-LCM-UV) and measured at FWHM. The OH fluorescence and OH* chemiluminescence signals were captured using an intensified CMOS camera (LV IRO X intensifier and Imager M-lite 5M, 2448 × 2048 px with $3.45 \times 3.45$ μm), coupled with a high transmissivity (80%) narrowband bandpass filter with a 25 nm FWHM bandwidth centred at 320 nm. This allowed to suppress the laser beam wavelength while capturing the OH $A^2\Sigma^+$-$X^2\Pi$ (0,0) emission from both OH PLIF and OH* chemiluminescence. PLIF measurements were taken using an intensifier gate of 100 ns, whereas chemiluminescence was subsequently recorded with a gate of 100 $\mu$s and the laser turned off. The camera was mounted around 70 cm away from the probe volume, achieving a spatial calibration of 29.33 px/mm. No binning was applied in order to maximise spatial resolution, leading to a line spread function (LSF) with a characteristic width of 0.197 mm and an effective optical uncertainty ranging from 0.128 to 0.166 mm across equivalence ratio. These values are comparable to the smallest flame thickness under these conditions ($\delta_L^0 = 0.30$ mm), resulting in spatial averaging that affects both peak position and peak width. Finally, a laser power scan confirmed that the fluorescence remained in the linear regime. A schematic of the experimental setup is provided in Fig. 5.

### 2.5. Image processing and peak determination

For each excitation wavelength, 200 single-shot OH PLIF images were averaged, sheet-corrected, and normalised between 0 and 1 prior to subtraction. The sheet correction was performed using DAVIS 11 flat field correction function toolbox. The ∇OH was obtained by applying the MATLAB `imgradient()` function to the averaged fluorescence signal from the $Q_1(8)$ excitation line. Similarly, 200 single-shot OH* chemiluminescence images were averaged, and Abel inversion was applied instead of subtraction, to reduce the line-of-sight integration limitations.

The resulting intensity distribution of these images was analysed along a line drawn perpendicular to the flame front (*dashed* in Fig. 6, left) in the quasi-planar region. Only this region was considered, since the curved regions near the flame tip and rim are subject to strain effects that alter the flame structure relative to freely propagating laminar flames obtained in numerical simulations [55]. To improve statistical reliability, eight additional lines were traced within a range of ± 0.85 mm (between the *dotted lines* in Fig. 6, left) around the central line. This allowed to calculate mean and standard deviation of the peak position and width across the flame, as well as the SNR.

To ensure a consistent spatial reference between the experimental measurements and the 1D numerical simulations in Section 2.3, the spatial grid of the simulations was aligned with the experimental data by matching the OH* peak location and scaling according to the spatial calibration of 29.33 px/mm, defined in Section 2.4. This procedure establishes a common reference for evaluating the markers locations and for computing normalised peak-to-peak distance and peak width with respect to HRR extracted from the experiments.

Fig. 6 demonstrates this procedure for two example conditions: a lean flame ($\phi = 0.60$) showing (−)OH alongside OH* (Fig. 6(a)), and a rich flame ($\phi = 1.20$) showing (−)OH alongside ∇OH (Fig. 6(b)). Each panel includes the peak detection for (−)OH (i) and for OH* or ∇OH (iii) along with their respective standard deviations (*shaded region*), as well as the average intensity profiles overlapped with the simulated HRR (ii).

As discussed in Section 2.4, the analysis is based on average images under the assumption of an axisymmetrical steady laminar flame. While shot-to-shot fluctuations arising from turbulence or flame instabilities can, in general, lead to smearing and reduced accuracy in flame front detection, their impact was limited in the present experiments. Except for the lean blow-off case at $\phi = 0.50$, where flame oscillations exhibited a variance coefficient of 12%, fluctuations remained small with a variance coefficient of approximately 3%, indicating that the averaging assumption is appropriate for the conditions investigated.

## 3. Results and discussion

Fig. 7 presents the averaged images for the range of equivalence ratios examined. The first row contains the OH PLIF fields obtained using the $A^2\Sigma^+$-$X^2\Pi$ (1,0) $Q_1(8)$ excitation line and the second row the corresponding (−)OH fields produced by subtracting the $Q_1(4)$ excitation line. The third and fourth rows display the gradient derived from the $Q_1(8)$ fluorescence and the Abel-inverted OH* chemiluminescence respectively. The sequence illustrates the effect of increasing equivalence ratio while maintaining constant thermal power (constant fuel flow rate), for a hydrogen flame. Increasing $\phi$ widens the flame cone and shifts the reaction zone closer to the burner rim, driven by the combined effect of higher laminar flame speed and reduced air flow rate.

In the lean cases ($\phi \leq 1.00$), an OH-depleted post flame region is observed, characterised by an absence of OH caused by gas expansion following rapid heat release in the reaction zone [56]. This feature is absent in the OH* chemiluminescence images, as no reactions take place in this region to chemically excite OH. Under rich conditions ($\phi \geq 1.05$), an outer diffusion flame is formed [57], as the excess fuel reacts with surrounding ambient air, as discussed in Section 2.4. The OH excited emission from this secondary flame reduces the accuracy of peak position and width retrieval for all markers, as the inner premixed flame becomes comparatively dimmer. For instance, at $\phi = 1.30$, the inner premixed flame intensity obtained using the $Q_1(8)$ OH PLIF is 12.5% that of the outer diffusion flame. This effect is particularly pronounced for ∇OH, which is already limited by low SNR as commonly mentioned in literature [38,39].

Across all equivalence ratios, the OH fluorescence decay in the post-flame region responds differently to temperature at each excitation wavelength, resulting in distinct slopes that also produce a marker when the two images are subtracted. However, this variation in OH concentration across the diffusion layer produces broader highlighted zones with an average intensity that is 52.82% lower than in the premixed region, allowing the primary reaction zone to be distinguished from false positives where heat release is not present. At rich conditions, the marker intensity in the diffusion layer increases to 82.41% of that in the premixed region due to additional OH formation in the secondary diffusion flame, also associated with heat release. Nevertheless, the focus of this study remains on the premixed region, which can be better compared with the 1D simulations in Section 2.1.

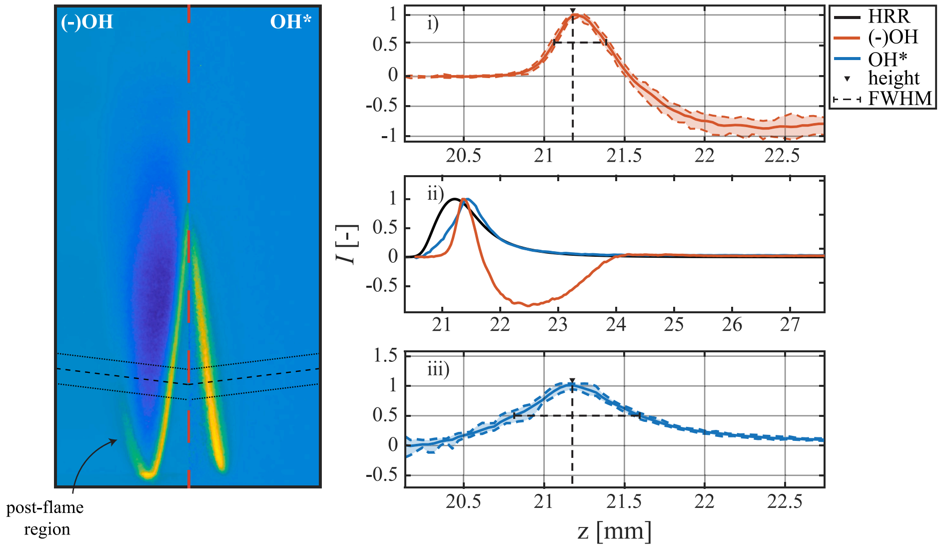

a) $\phi$ = 0.60

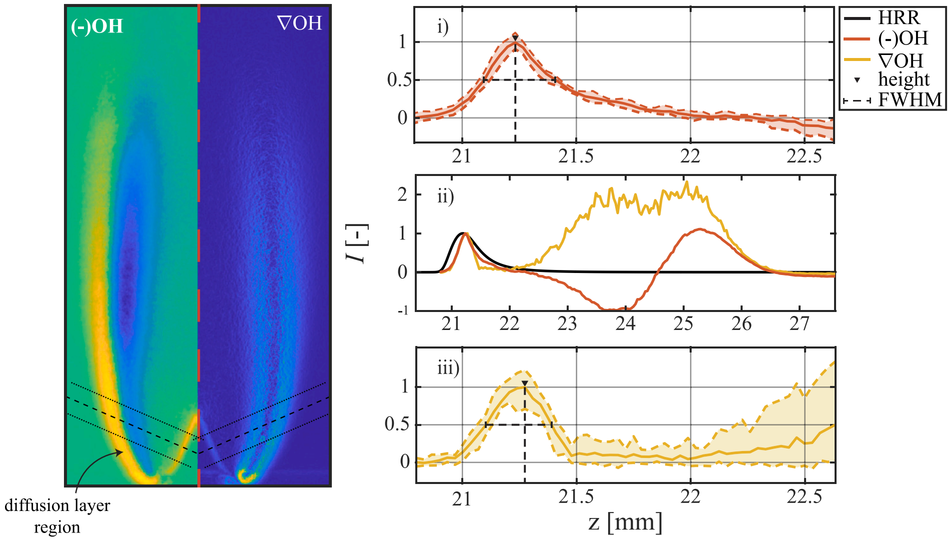

b) $\phi$ = 1.30

**Fig. 6.** Examples of the post-processing procedure used to determine the peak position and width of the markers in premixed $H_2$-air laminar flames. (a) Lean flame ($\phi = 0.60$) showing (−)OH together with OH*, and (b) Rich flame ($\phi = 1.30$) showing (−)OH together with ∇OH. For each condition, the region where the intensity profiles were traced is illustrated. The intensity distributions across the nine lines for (−)OH (i) and for OH* or ∇OH (iii) are shown, as well as the correspondent average intensity profiles (ii).

Each method also exhibits specific features in the experimentally obtained images. OH* maker appears broader with respect to (−)OH and ∇OH, due to its line-of-sight nature, which inherently widens the apparent flame front, as will be seen later in Fig. 8. The ∇OH fields display speckling within the reaction zone, reflecting the limited SNR. In the (−)OH images, residual differences in sheet corrections between the two excitation wavelengths are visible, particularly at $\phi$ = 0.80. Flame oscillations near lean blow-off ($\phi$ = 0.50) also appear more clearly, as the two averaged images used for subtraction are not acquired simultaneously, meaning slight differences in flame position relative to the average are amplified. This leads to spatial smearing near the flame tip, resulting in the absence of a clearly identifiable (−)OH marker in that region. Furthermore, these oscillations near lean blow-off introduce small departures from the axisymmetry required for Abel inversion of the OH* signal, which can affect the accuracy of the measurement. However, in the present case, these spatial oscillations (~0.137 mm) remain under the effective spatial resolution of the imaging system (see Section 2.4) and are therefore not expected to significantly affect the extracted results.

Tables 2 and 3 summarise the peak position and width obtained experimentally for the proposed (−)OH marker, Abel-inverted OH* chemiluminescence, and ∇OH, along with their respective standard deviations. These standard deviations were obtained by scanning the intensity along nine lines across the quasi-planar section of the premixed flame, as described in Section 2.5. These results were also converted into normalised peak-to-peak distance and normalised width, both relative to HRR, to ensure consistency with the definitions introduced in Section 2.3 (see Fig. 8). In the corresponding figures, the standard deviation between the acquired points were interpolated using a piecewise cubic polynomial, preserving the measured values at each point.

The normalised peak-to-peak distances follow trends consistent with the numerical results in Section 2.3. This is particularly evident for OH* and (−)OH, where the latter transitions from being closer to HRR than OH* at lean conditions to further away as $\phi$ increases. In contrast, a notable discrepancy appears for ∇OH. Experimentally, it becomes the marker located furthest from the HRR peak for $\phi \geq 0.60$

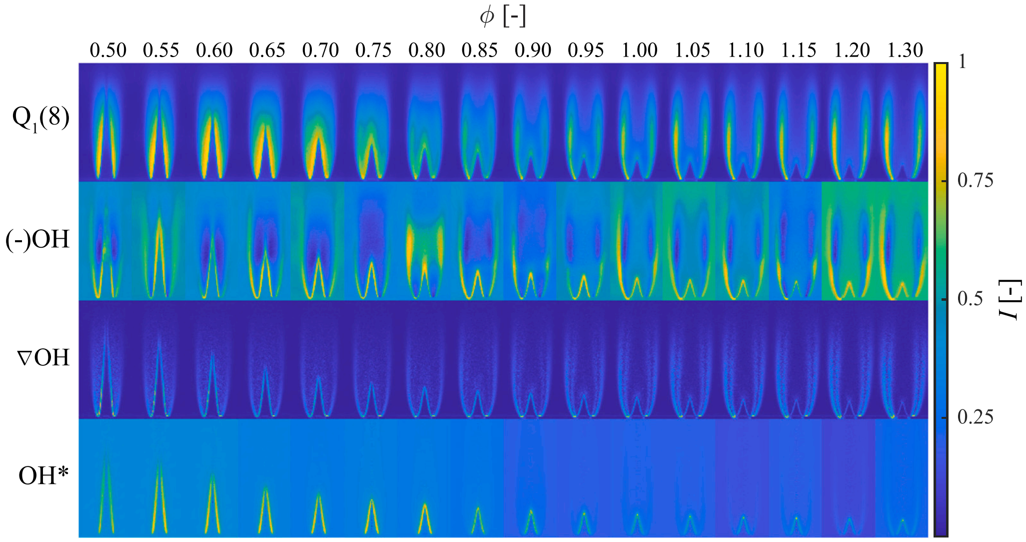

**Fig. 7.** $A^2\Sigma^+$-$X^2\Pi$ (1,0) $Q_1(8)$ OH PLIF (*first row*), (−)OH ($Q_1(4)$-$Q_1(8)$ subtraction, *second row*), ∇OH (*third row*), and Abel-inverted OH* Chemiluminescence (*fourth row*), shown for laminar premixed $H_2$-air Bunsen flames with equivalence ratios from $\phi = 0.5$ to 1.3 (left to right).

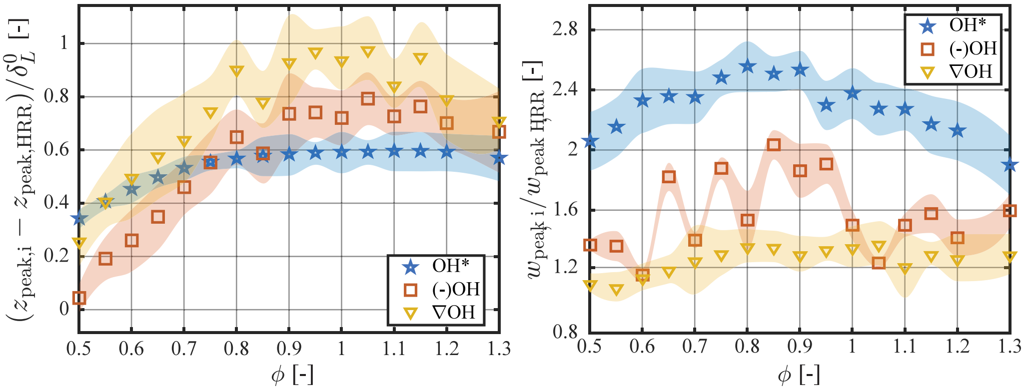

a)

b)

**Fig. 8.** (a) Normalised peak-to-peak distance and (b) normalised peak-width of OH*, (−)OH and ∇OH relative to HRR equivalence ratios from $\phi$ = 0.5 to 1.3 obtained experimentally in a laminar premixed $H_2$-air Bunsen flame.

**Table 2**

Experimentally measured peak position ($z_{\text{peak}}$) for (−)OH, OH*, and ∇OH along 9 lines normal to the quasi-planar region of a premixed $H_2$-air Bunsen flame for $\phi = 0.5$ to 1.3.

| $\phi$ | OH* $z_{\text{peak}}$ [mm] | (−)OH $z_{\text{peak}}$ [mm] | ∇OH $z_{\text{peak}}$ [mm] |
|---|---|---|---|
| 0.50 | 21.340 ± 0.017 | 21.207 ± 0.043 | 21.306 ± 0.045 |
| 0.55 | 21.299 ± 0.011 | 21.216 ± 0.039 | 21.303 ± 0.043 |
| 0.60 | 21.271 ± 0.018 | 21.203 ± 0.042 | 21.290 ± 0.057 |
| 0.65 | 21.256 ± 0.012 | 21.207 ± 0.042 | 21.287 ± 0.058 |
| 0.70 | 21.247 ± 0.015 | 21.225 ± 0.034 | 21.285 ± 0.055 |
| 0.75 | 21.240 ± 0.010 | 21.240 ± 0.038 | 21.305 ± 0.040 |
| 0.80 | 21.234 ± 0.011 | 21.261 ± 0.033 | 21.344 ± 0.033 |
| 0.85 | 21.230 ± 0.023 | 21.234 ± 0.036 | 21.298 ± 0.034 |
| 0.90 | 21.227 ± 0.025 | 21.276 ± 0.049 | 21.341 ± 0.054 |
| 0.95 | 21.225 ± 0.014 | 21.274 ± 0.030 | 21.350 ± 0.024 |
| 1.00 | 21.223 ± 0.025 | 21.264 ± 0.033 | 21.336 ± 0.038 |
| 1.05 | 21.220 ± 0.015 | 21.284 ± 0.032 | 21.345 ± 0.038 |
| 1.10 | 21.218 ± 0.023 | 21.260 ± 0.023 | 21.299 ± 0.029 |
| 1.15 | 21.215 ± 0.023 | 21.268 ± 0.030 | 21.329 ± 0.038 |
| 1.20 | 21.211 ± 0.022 | 21.246 ± 0.030 | 21.276 ± 0.050 |
| 1.30 | 21.202 ± 0.026 | 21.232 ± 0.047 | 21.247 ± 0.034 |

**Table 3**

Experimentally measured peak width ($w_{\text{peak}}$) for (−)OH, OH*, and ∇OH along 9 lines normal to the quasi-planar region of a premixed $H_2$-air Bunsen flame for $\phi = 0.5$ to 1.3.

| $\phi$ | OH* $w_{\text{peak}}$ [mm] | (−)OH $w_{\text{peak}}$ [mm] | ∇OH $w_{\text{peak}}$ [mm] |
|---|---|---|---|
| 0.50 | 0.692 ± 0.066 | 0.460 ± 0.012 | 0.376 ± 0.021 |
| 0.55 | 0.661 ± 0.060 | 0.418 ± 0.031 | 0.335 ± 0.030 |
| 0.60 | 0.666 ± 0.061 | 0.335 ± 0.014 | 0.331 ± 0.026 |
| 0.65 | 0.637 ± 0.049 | 0.493 ± 0.025 | 0.327 ± 0.026 |
| 0.70 | 0.607 ± 0.045 | 0.362 ± 0.014 | 0.329 ± 0.059 |
| 0.75 | 0.619 ± 0.031 | 0.469 ± 0.018 | 0.329 ± 0.038 |
| 0.80 | 0.620 ± 0.041 | 0.372 ± 0.047 | 0.331 ± 0.027 |
| 0.85 | 0.595 ± 0.028 | 0.483 ± 0.023 | 0.323 ± 0.025 |
| 0.90 | 0.591 ± 0.030 | 0.435 ± 0.042 | 0.306 ± 0.028 |
| 0.95 | 0.529 ± 0.038 | 0.439 ± 0.030 | 0.309 ± 0.018 |
| 1.00 | 0.541 ± 0.039 | 0.342 ± 0.023 | 0.309 ± 0.031 |
| 1.05 | 0.513 ± 0.040 | 0.282 ± 0.007 | 0.312 ± 0.033 |
| 1.10 | 0.509 ± 0.031 | 0.337 ± 0.018 | 0.276 ± 0.048 |
| 1.15 | 0.484 ± 0.043 | 0.352 ± 0.029 | 0.293 ± 0.017 |
| 1.20 | 0.473 ± 0.044 | 0.315 ± 0.027 | 0.286 ± 0.035 |
| 1.30 | 0.421 ± 0.044 | 0.354 ± 0.025 | 0.291 ± 0.030 |

(0.16-1.12 $\delta_L^0$), whereas the simulations predicted it to lie closest (0.10-0.21 $\delta_L^0$). This difference could be partly explained by the neglect of collisional quenching in the numerical simulations, as quenching modifies the OH LIF signal. In the reaction zone, two competing effects influence quenching: increasing concentration of collisional partners (O, H, $H_2O$, NO, etc.) and the rise in temperature. This likely leads to a non-monotonic variation of quenching rate across the flame front, which not only can reduce the signal intensity but can also alter the gradient of the OH profile. This, coupled with limited camera resolution that introduces spatial averaging, can shift the peak location of ∇OH towards the product side. In addition, the lower SNR (22 compared to 47 and 60 for (−)OH and OH* respectively) increases the uncertainty of the measurement. Although the standard deviations for all markers are of similar magnitude, OH* shows an increase at higher equivalence ratios. This corresponds to the appearance of the secondary diffusion flame, which weakens the apparent intensity of the inner premixed flame in line-of-sight measurements, as the diffusion flame sits between the camera and the inner premixed flame. Finally, the limited spatial resolution detailed in Section 2.4 also affects the results, as the uncertainty of the measurement ranges from 0.128 mm to 0.166 mm across conditions, which is comparable to the smallest laminar flame thickness at these conditions ($\delta_L^0 = 0.30$ mm).

Fig. 8(b) illustrates the normalised peak widths ($w_{peak}$). OH* generally follows a simulated trend to the numerical simulations, although the approximately constant behaviour expected at richer conditions is not fully reproduced. This discrepancy could be again justified by the formation of a secondary flame at these conditions. Finally, as the only line-of-sight technique studied, it naturally yields the broadest marker with an average value of $2.29 w_{\mathrm{HRR}}$, even after Abel inversion. For ∇OH, experiments resemble a similar trend to that observed in the simulations but over distinct ranges ($1.02\text{-}1.53 w_{\mathrm{HRR}}$ and $0.65\text{-}0.74 w_{\mathrm{HRR}}$, respectively). This discrepancy can be attributed to both experimental effects (e.g. flame flickering, heat losses to the burner rim and camera resolution) and the limited ability of the numerical simulations to fully describe LIF in experimental conditions. The (−)OH marker displays an average peak width almost as close to HRR as ∇OH ($1.57 w_{\mathrm{HRR}}$) and a comparable average standard deviation to the other markers (0.125 mm, compared with 0.170 and 0.098 mm for OH* and ∇OH, respectively). However it presents sharp point-to-point fluctuations. These are attributed to the use of a single laser system for this demonstration, which required the least and most temperature-dependent excitation lines to be acquired sequentially rather than simultaneously. As (−)OH is derived from two images acquired at different times, it exhibits stronger fluctuations. This limitation can be addressed by acquiring the two excitation wavelengths simultaneously, as explained in the Section 4.

To conclude the analysis, Fig. 9 illustrates how the numerically obtained normalised peak-to-peak distance and normalised peak-width of the proposed (−)OH method related to the one measured experimentally. A linear regression was applied to assess how well the two datasets correlate. The normalised peak-to-peak distance shows the strongest agreement, with a slope of 0.7170 and a small average residual of 0.0758, indicating that this quantity is reasonably reproduced by the simulations. However, the normalised peak width shows poor correlation, with a slope of 0.9780 and a large average residual of 2.2081, indicating that the simulations are not able to capture the full physics of the proposed marker. This highlights that comparisons between simulated and experimental fluorescence-based markers would benefit from LIF profiles that better describe experimentally obtained OH-PLIF profiles, as further discussed in the Section 4.

## 4. Outlook

The present study demonstrates the feasibility of subtracting two fluorescence images acquired with two wavelengths with different temperature dependencies to create a marker across the flame front. This was achieved under laminar, axisymmetric conditions as a first step, allowing the method to be validated using averaged images despite sequential acquisition of the two excitation lines.

These promising results motivate the further development of the technique into turbulent flames. This will be achieved by employing an additional synchronised laser with an inter-pulse delay shorter than the Kolmogorov time scale ($\tau_\varepsilon$), as commonly implemented in two-line PLIF measurements [40]. For instance, a 5 cm burner with Re = 20,000 has $\tau_\varepsilon \sim 60$ $\mu$s, assuming $\varepsilon = U^3/L$, where $\varepsilon$ is the turbulent kinetic energy dissipation rate, $U$ the characteristic flow velocity and $L$ the characteristic length scale [58]. This timescale is still several orders of magnitude longer than the fluorescence timescale (10 ns [32]) and the 100 ns intensifier gate used to capture fluorescence (see Section 2.4). Such synchronised dual-laser approaches have already been demonstrated in turbulent flames using two-line PLIF [40,59] and combined OH×$CH_2O$ PLIF measurements [60].

Furthermore, as evidenced by the comparison between simulations and experiments in Fig. 9, the current modelling approach is not able to fully reproduce the (−)OH marker. One of the reasons is the simplification of neglecting collisional quenching, affecting the predicted OH fluorescence distribution and consequently, both (−)OH and ∇OH markers. Therefore, expanding LIFSIM to better describe LIF and to include an OH collisional quenching model (e.g. the harpooned mechanism proposed by Paul [61]) would allow for a better physical description of the proposed marker.

With these extensions, the proposed method could be better interpreted and provide a path towards time-resolved flame front diagnostics in turbulent and non-axisymmetric hydrogen flames, contributing to the ongoing discussion on suitable markers for experimental and numerical characterisation of hydrogen flames.

## 5. Conclusion

The current study proposes a new method to generate a spatially resolved marker across the flame front by subtracting fluorescence signals from two OH excitation lines with different temperature dependencies. To achieve this, the temperature dependence of several OH transitions was quantified using LIFSIM over 1100–2400 K, through an OH number density-weighted average. This analysis identified the $A^2\Sigma^+–X^2\Pi$ (1,0) $Q_1(8)$ as the least temperature-dependent and $A^2\Sigma^+–X^2\Pi$ (1,0) $Q_1(4)$ as the most temperature-dependent for most equivalence ratios.

The method was evaluated numerically using one-dimensional freely propagating premixed $H_2$–air flame simulations in combination with LIFSIM outputs. This confirmed that subtracting the computed fluorescence from the two selected transitions produced a distinct peak that successfully marks the flame front. Additionally, the peak position and width of this marker were compared against HRR, OH*, and ∇OH to characterise how the proposed technique differs from established diagnostics.

Experimental validation was performed by collecting OH fluorescence in a laminar premixed $H_2$-air Bunsen flame. The fluorescence at the selected excitation wavelengths was acquired and subtracted to obtain the (−)OH signal, which highlighted both the flame front and the outer diffusion layer due to the gradual decay of OH across it. From these images, intensity profiles along perpendicular lines to the flame front were used to extract the average peak position and width within the premixed zone. Equivalent analyses were performed for Abel-inverted OH* chemiluminescence and ∇OH PLIF for the least temperature-dependent line ($A^2\Sigma^+–X^2\Pi$ (1,0) $Q_1(8)$). The OH* profiles was used to match the spatial grid of both simulations and experiments.

The proposed (−)OH marker reproduced the overall behaviour expected from the simulations in terms of normalised peak-to-peak distance and closely followed the trend observed for OH*. Experimentally, (−)OH was also found to lie closer to the HRR than ∇OH ($0.01\text{-}0.89\delta_L^0$ compared with 0.16-1.12 $\delta_L^0$), a difference partly attributed to the lower SNR of the gradient-based technique. The normalised

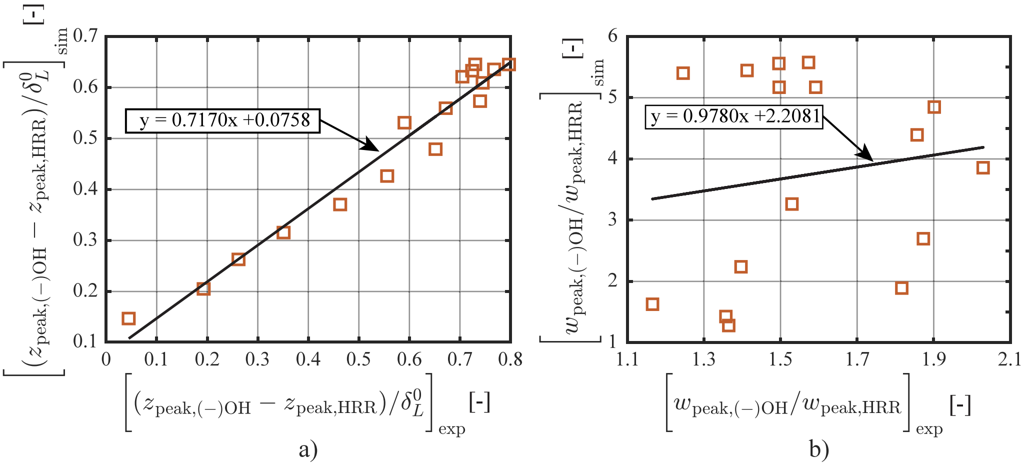

**Fig. 9.** Comparison of experimental and simulated (a) normalised peak-to-peak distance and (b) normalised peak-width of (−)OH relative to HRR for equivalence ratios from $\phi = 0.5$ to 1.3 obtained in a laminar premixed $H_2$-air Bunsen flame.

peak widths revealed larger deviations from the numerical predictions, with (−)OH exhibiting sharper point-to-point fluctuations due to the non-simultaneous acquisition of the two excitation lines, while OH* naturally produced a broader marker due to its line-of-sight nature, even after Abel inversion. Despite these differences, the average peak widths of (−)OH, OH* and ∇OH remained reasonably close to that of HRR. Thus, this study demonstrated that the proposed method successfully generates a robust flame front marker across premixed hydrogen flames.

The main takeaways from this study are:

1. Subtracting OH PLIF images from two excitation lines with distinct temperature dependencies creates a reliable marker within the flame front.
2. The proposed method offers improvements over OH* and ∇OH, providing a spatially resolved marker closer to the HRR and with stronger SNR, allowing for better detection of the flame front. It is also suitable for hydrogen flames, where $CH_2O$ PLIF is not applicable due to the absence of carbon.
3. Numerical and experimental comparisons reveal decent agreement for the normalised peak-to-peak distance of the proposed marker, while discrepancies in peak width highlight its sensitivity to experimental effects and numerical modelling assumptions.

## CRediT authorship contribution statement

**André Silva Correia:** Writing – original draft, Visualization, Validation, Software, Methodology, Investigation, Formal analysis, Data curation, Conceptualization. **Francesco Mazza:** Writing – review & editing, Methodology, Conceptualization. **Leonardo Castellanos:** Writing – review & editing, Methodology, Conceptualization. **Arvind Gangoli Rao:** Writing – review & editing, Supervision. **Francesca De Domenico:** Writing – review & editing, Supervision, Methodology, Conceptualization.

## Declaration of competing interest

The authors declare that they have no known competing financial interests or personal relationships that could have appeared to influence the work reported in this paper.

## Acknowledgements

We gratefully acknowledge the financial support provided by the Dutch Research Council (NWO), obtained through a VENI grant in the Applied and Engineering Sciences domain (AES2022 - 20312). In addition, we thank our colleague S. Link for the valuable technical assistance during the experiments, as well as G. Ferrante and R. Sampat for the insightful discussions on this work.

## References

[1] Lee H, Romero J. Climate change 2023: Synthesis report. Geneva, Switzerland: IPCC; 2023, p. 35–115, Available at: https://www.ipcc.ch/report/ar6/syr/downloads/report/IPCC_AR6_SYR_LongerReport.pdf, [Accessed October 2025].

[2] Speth Raymond L, Ghoniem Ahmed F. Using a strained flame model to collapse dynamic mode data in a swirl-stabilized syngas combustor. Proc Combust Inst 2009;32(2):2993–3000.

[3] Dinesh KKJ Ranga, Shalaby H, Luo KH, Van Oijen JA, Thévenin D. High hydrogen content syngas fuel burning in lean premixed spherical flames at elevated pressures: Effects of preferential diffusion. Int J Hydrog Energy 2016;41(40):18231–49.

[4] Hu Yong, Kurose Ryoichi. Large-eddy simulation of turbulent autoigniting hydrogen lifted jet flame with a multi-regime flamelet approach. Int J Hydrog Energy 2019;44(12):6313–24.

[5] Johannessen Birgitte, North Andrew, Dibble Robert, Løvås Terese. Experimental studies of autoignition events in unsteady hydrogen–air flames. Combust Flame 2015;162(9):3210–9.

[6] De Giorgi Maria Grazia, Campilongo Stefano, Ficarella Antonio, De Falco Gianluigi, Commodo Mario, D'Anna Andrea. Energies 2017;352.

[7] Hathout JP, Fleifil M, Annaswamy AM, Ghoniem AF. Heat-release actuation for control of mixture-inhomogeneity-driven combustion instability. Proc Combust Inst 2000;28(1):721–30.

[8] Candel Sébastien. Combustion dynamics and control: Progress and challenges. Proc Combust Inst 2002;29(1):1–28.

[9] Ayoola BO, Balachandran R, Frank JH, Mastorakos E, Kaminski CF. Spatially resolved heat release rate measurements in turbulent premixed flames. Combust Flame 2006;144(1–2):1–16.

[10] Liu Fushui, Bao Xiuchao, Gu Jiayi, Chen Rui. Onset of cellular instabilities in spherically propagating hydrogen-air premixed laminar flames. Int J Hydrog Energy 2012;37(15):11458–65.

[11] Sun Zuo-Yu, Liu Fu-Shui, Bao Xiu-Chao, Liu Xing-Hua. Research on cellular instabilities in outwardly propagating spherical hydrogen-air flames. Int J Hydrog Energy 2012;37(9):7889–99.

[12] Ye Pedro, Erhard Jannick, Welch Cooper, Shi Hao, Dreizler Andreas, Böhm Benjamin. Analysis of thermodiffusive instabilities and flame front wrinkling in a hydrogen-fueled engine. Proc Combust Inst 2025;41:105884.

[13] Guo Chengfei, Zhou Hao. Effect of hydrogen blending on thermoacoustic instability and flashback dynamics in partially premixed methane-air flames. Fuel 2025;393:135007.

[14] Erkal Burak. Thermoacoustic instabilities in hydrogen-methane flames. Proc ASME Turbo Expo 2025;GT2025. V03BT04A001.

[15] zur Nedden PM, Eck MEG, Lückoff F, Panek Ł , Orchini A, Paschereit CO. Flame transfer function and emissions of a piloted single jet burner: influence of hydrogen content. J Eng Gas Turbines Power 2025.

[16] Marragou S, Palies P. Near-field mixing in a coaxial dual swirled injector. Flow, Turbul Combust 2025;114(2):241–60.

[17] Qi H, Zhang L. Investigation of flame response in a swirling micromix combustor. J Eng Gas Turbines Power 2024;146(12):121027.

[18] Chakraborti S, Bawne SK. A review on advancement in strategies for low-NOx hydrogen combustion with micromix technology. Aeronaut J 2025;129(1342):1461–85.

[19] Berger L, Schuh M. LES combustion model for premixed turbulent hydrogen flames with thermodiffusive instabilities: a priori and a posteriori analysis. J Fluid Mech 2025;897:A20.

[20] Schuh M, Berger L. Extended flame transfer function model for hydrogen combustion. Proc Combust Inst 2025;38(4):5415–23.

[21] Kojima Jun, Ikeda Yuji, Nakajima Tsuyoshi. Spatially resolved measurement of OH*, CH*, and C2* chemiluminescence in the reaction zone of laminar methane/air premixed flames. Proc Combust Inst 2000;28(2):1757–64.

[22] Baumgardner Marc E, Graves Anthony. Temperature, soot, and OH*/CH* chemiluminescence measurements of partially-premixed CO2-diluted propane flames on a linear Hencken burner. Fuel 2022;328:125178.

[23] Tian Xinming, Yang Jiabao, Guo Qinghua, Yan Shuai, Gong Yan, Yu Guangsuo. Study on CO2* chemiluminescence of CH4/O2 co-flow diffusion flame based on the chemical kinetic mechanism. Fuel 2024;359:130484.

[24] Schefer RW, Kulatilaka WD, Patterson BD, Settersten TB. Visible emission of hydrogen flames. Combust Flame 2009;156(6):1234–41.

[25] Yoo SW, Law CK, Tse SD. Chemiluminescent OH* and CH* flame structure and aerodynamic scaling of weakly buoyant, nearly spherical diffusion flames. Proc Combust Inst 2002;29(2):1663–70.

[26] Schiavone Francesco G, Aniello Andrea, Riber Eleonore, Schuller Thierry, Laera Davide. On the adequacy of OH* as heat release marker for hydrogen–air flames. Proc Combust Inst 2024;40(1):105248.

[27] Schiavone Francesco G, Torresi Marco, Camporeale Sergio M, Laera Davide. Impact of the operating conditions on the OH* distribution and its correlation with the heat release rate in hydrogen–air flames. Combust Flame 2025;282:114452.

[28] Wiseman Samuel M, Brear Michael J, Gordon Robert L, Marusic Ivan. Measurements from flame chemiluminescence tomography of forced laminar premixed propane flames. Combust Flame 2017;183:1–14.

[29] Turner Mattias A, Paschal Tyler T, Parajuli Pradeep, Kulatilaka Waruna D, Petersen Eric L. Resolving flame thickness using high-speed chemiluminescence imaging of OH* and CH* in spherically expanding methane–air flames. Proc Combust Inst 2021;38(2):2101–8.

[30] Dynamics Dantec. LIF vs. Chemiluminescence measurements for flame front studies. 2025, [Accessed 06 March 2025].

[31] Eckbreth AC. Laser diagnostics for combustion temperature and species. 3st ed.. CRC Press; 1996.

[32] Kienle R, Lee MP, Kohse-Höinghaus Katharina. A detailed rate equation model for the simulation of energy transfer in OH laser-induced fluorescence. Appl Phys B 1996;62:583–99.

[33] Najm Habib N, Paul Phillip H, Mueller Charles J, Wyckoff Peter S. On the adequacy of certain experimental observables as measurements of flame burning rate. Combust Flame 1998;113(3):312–32.

[34] Fayoux Amélie, Zähringer K, Gicquel Olivier, Rolon Juan-Carlos. Experimental and numerical determination of heat release in counterflow premixed laminar flames. Proc Combust Inst 2005;30(1):251–7.

[35] Ayoola BO, Balachandran R, Frank JH, Mastorakos E, Kaminski CF. Spatially resolved heat release rate measurements in turbulent premixed flames. Combust Flame 2006;144(1):1–16.

[36] Gordon Robert L, Masri Assaad R, Mastorakos Epaminondas. Heat release rate as represented by [OH]×[CH2O] and its role in autoignition. Combust Theory Model 2009;13(4):645–70.

[37] Zheng Yutao, Weller Lee, Hochgreb Simone. Instantaneous flame front identification by mie scattering vs. OH PLIF in low turbulence bunsen flame. Exp Fluids 2022;63(5):79.

[38] Boxx I, Slabaugh C, Kutne P, Lucht RP, Meier W. 3kHz PIV/OH-PLIF measurements in a gas turbine combustor at elevated pressure. Proc Combust Inst 2015;35(3):3793–802.

[39] Yue Han, Cai Guo-Biao, Xu Xu, Renou Bruno, Boukhalfa Abdelkrim. A conditioned level-set method with block-division strategy to flame front extraction based on OH-PLIF measurements. Chin Phys B 2014;23(5):058901.

[40] Giezendanner-Thoben Robert, Meier Ulrich, Meier Wolfgang, Aigner Manfred. Flow, Turbul Combust 2005;317–33.

[41] El Moussawi Abbas, Karaminejad Sadrollah, Menser Jan, Bessler Wolfgang G, Dreier Thomas, Endres Torsten, Schulz Christof. Lifsim, a modular laser-induced fluorescence code for concentration and temperature analysis of diatomic molecules. Appl Phys B 2025;131(4):72.

[42] Goodwin David G, Moffat Harry K, Schoegl Ingmar, Speth Raymond L, Weber Bryan W. Cantera: An object-oriented software toolkit for chemical kinetics, thermodynamics, and transport processes. 2023, Version 3.0.0, https://www.cantera.org.

[43] Smith Gregory P, Golden David M, Frenklach Michael, Moriarty Nigel W, Eiteneer Boris, Goldenberg Mikhail, Bowman C Thomas, Hanson Ronald K, Song Soonho, William C. Gardiner Jr, Lissianski Vitali V, Qin Zhiwei. GRI-Mech Chemical Kinetic Mechanism.

[44] Kathrotia Trupti, Fikri M, Bozkurt M, Hartmann M, Riedel U, Schulz C. Study of the H+ O+ M reaction forming OH*: Kinetics of OH* chemiluminescence in hydrogen combustion systems. Combust Flame 2010;157(7):1261–73.

[45] Zhao Mengmeng, Buttsworth David, Choudhury Rishabh. Experimental and numerical study of OH* chemiluminescence in hydrogen diffusion flames. Combust Flame 2018;197:369–77.

[46] Graña-Otero José, Mahmoudi Siamak. Excited OH kinetics and distribution in H2 premixed flames. Fuel 2019;255:115750.

[47] He Lei, Guo Qinghua, Gong Yan, Wang Fuchen, Yu Guangsuo. Investigation of OH* chemiluminescence and heat release in laminar methane–oxygen co-flow diffusion flames. Combust Flame 2019;201:12–22.

[48] Heard Dwayne E, Henderson David A. Quenching of OH (a 2 $\Sigma$+, v′=0) by several collision partners between 200 and 344 K. Cross-section measurements and model comparisons. Phys Chem Chem Phys 2000;2(1):67–72.

[49] German KR. Collision and quenching cross sections in the A 2$\Sigma$+ state of OH and OD. J Chem Phys 1976;64(10):4065–8.

[50] Silva Correia André. LIFTempdependence. 2025, version 1.0.0. 4TU.ResearchData. software.

[51] Tu Xiaobo, Wang Linsen, Qi Xinhua, Yan Bo, Mu Jinhe, Chen Shuang. Effects of temperature and pressure on OH laser-induced fluorescence exciting A–X (1, 0) transition at high pressures. Chin Phys B 2020;29(9):093301.

[52] Docquier Nicolas, Candel Sébastien. Combustion control and sensors: a review. Prog Energy Combust Sci 2002;28(2):107–50.

[53] Bunev Valery Aleksandrovich, Panfilov Viktor Nikolaevich, Babkin Vyacheslav Stepanovich. Role of atomic hydrogen diffusion in a hydrogen flame. Combust Explos Shock Waves 2007;43(2):125–31.

[54] Kwon OC, Faeth GM. Flame/stretch interactions of premixed hydrogen-fueled flames: measurements and predictions. Combust Flame 2001;124(4):590–610.

[55] Choi Chun W, Puri Ishwar K. Contribution of curvature to flame-stretch effects on premixed flames. Combust Flame 2001;126(3):1640–54.

[56] Hu S, Gao J, Gong C, Zhou Y, Bai dan XS, Li ZS, Alden M. Appl Energy 2018;149–58.

[57] Fu Jin, Tang Chenglong, Jin Wu, Huang Zuohua. Effect of preferential diffusion and flame stretch on flame structure and laminar burning velocity of syngas Bunsen flame using OH-PLIF.

[58] Pope Stephen B. Turbulent flows. Meas Sci Technol 2001;12(11):2020–1.

[59] Tao Chao, Zhang Chi, An Qiang, Xue Xin. Temperature field measurements in swirl spray flames using two-line planar laser induced fluorescence thermometry. J Eng Gas Turbines Power 2025;147(3):031009.

[60] Fugger Christopher A, Roy Sukesh, Caswell Andrew W, Rankin Brent A, Gord James R. Structure and dynamics of CH2O, OH, and the velocity field of a confined bluff-body premixed flame, using simultaneous PLIF and PIV at 10 kHz. Proc Combust Inst 2019;37(2):1461–9.

[61] Paul PH. A model for temperature-dependent collisional quenching of OHA2+. J Quant Spectrosc Radiat Transfer 1994;51(3):511–24.